

Kinematics of Abdominal Aortic Aneurysms

Mostafa Jamshidian*, Adam Wittek, Saeideh Sekhavat, Karol Miller

Intelligent Systems for Medicine Laboratory, The University of Western Australia, Perth,
Western Australia, Australia

A search in Scopus within “Article title, Abstract, Keywords” unveils 2,444 documents focused on the biomechanics of Abdominal Aortic Aneurysm (AAA), mostly on AAA wall stress. Only 24 documents investigated AAA kinematics, an important topic that could potentially offer insights into the biomechanics of AAA. In this paper, we present an image-based approach for patient-specific, in vivo, and non-invasive AAA kinematic analysis using patient’s time-resolved 3D computed tomography angiography (4D CTA) images. Our approach relies on regularized deformable image registration for estimating wall displacement, estimation of the local wall strain as the ratio of its normal displacement to its local radius of curvature, and local surface fitting with non-deterministic outlier detection for estimating the wall radius of curvature. We verified our approach against synthetic ground truth image data created by warping a 3D CTA image of AAA using a realistic displacement field obtained from a finite element biomechanical model. We applied our approach to assess AAA wall displacements and strains in ten patients. Our kinematic analysis results indicated that the 99th percentile of circumferential wall strain, among all patients, ranged from 3.16% to 7.31%, with an average of 5.36% and a standard deviation of 1.28%.

Keywords: Abdominal aortic aneurysm, Kinematics, Registration, Patient-specific analysis

* Corresponding author.

E-mail address: mostafa.jamshidian@uwa.edu.au (M. Jamshidian).

1. Introduction

Abdominal aortic aneurysm (AAA) is a permanent and irreversible dilation of the lower aorta that is asymptomatic and usually diagnosed incidentally during imaging for other health conditions. While asymptomatic, AAA can expand to the point of rupture if left untreated, leading to death in most cases (Wanhainen, Verzini et al. 2019, NICE 2020).

The current clinical practice for AAA management, based on the maximum diameter and its growth rate is a one-size-fits-all approach that recommends clinical intervention when the aneurysm diameter exceeds 5.5 cm in men and 5 cm in women, or when growth rates exceed 1 cm per year (Wanhainen, Verzini et al. 2019). The maximum diameter criteria may underestimate or overestimate the rupture risk in individual AAA patients, as evidenced by ruptured AAAs with diameters smaller than the critical diameter (Vorp 2007) and unruptured stable AAAs with diameters larger than the critical diameter (Darling, Messina et al. 1977, Wanhainen, Verzini et al. 2019, NICE 2020). Autopsy findings indicate that around 13% of AAAs with a maximum diameter of 5 cm or less experienced rupture, whereas 60% of AAAs larger than 5 cm in diameter remained unruptured (Kontopodis, Pantidis et al. 2016).

AAA biomechanics, particularly wall stress, has been extensively studied to customize disease management to individual patients (Fillinger, Raghavan et al. 2002, Fillinger, Marra et al. 2003, Vande Geest, Di Martino et al. 2006, Speelman, Bohra et al. 2007, Li, U-Ying-Im et al. 2008, Gasser, Auer et al. 2010, Indrakusuma, Jalalzadeh et al. 2016, Joldes, Miller et al. 2016, Joldes, Miller et al. 2017, Farotto, Segers et al. 2018, Miller, Mufty et al. 2020, Polzer, Gasser et al. 2020, Chung, Liang et al. 2022, Gasser, Miller et al. 2022, Singh, Moxon et al. 2023, Wang, Carpenter et al. 2023). While there is plenty of research on AAA stress analysis, literature on AAA kinematics is scarce.

Only a few research groups explored non-invasive, in-vivo measurement of AAA wall displacement and strain using sequential images at different phases in the cardiac cycle, often referred to as 4D images (Raut, Jana et al. 2014, Nagy, Csobay-Novák et al. 2015, Satriano, Rivolo et al. 2015, Wittek, Blase et al. 2017, Wang, Joannic et al. 2018, Wittek, Derwich et al. 2018, Cebull, Soepriatna et al. 2019, Derwich, Keller et al. 2023). (Raut, Jana et al. 2014) extracted the systolic and diastolic AAA geometries from MRI images using an in-house framework for image-based reconstruction of tessellated surfaces to evaluate wall

displacement and strain. (Witteck, Blase et al. 2017) combined speckle tracking algorithms with 4D ultrasound for measuring displacement and strain in AAA. (Nagy, Csobay-Novák et al. 2015) estimated AAA kinematic fields with an isogeometric shell analysis framework with smoothing to mitigate measurement inaccuracy. Based on fluid-structure interaction simulation, they assumed that the incremental displacement vector is normal to the AAA surface. (Satriano, Rivolo et al. 2015) used optical flow of time-wise consecutive images to first compute deformation and then aortic wall distensibility or deformability.

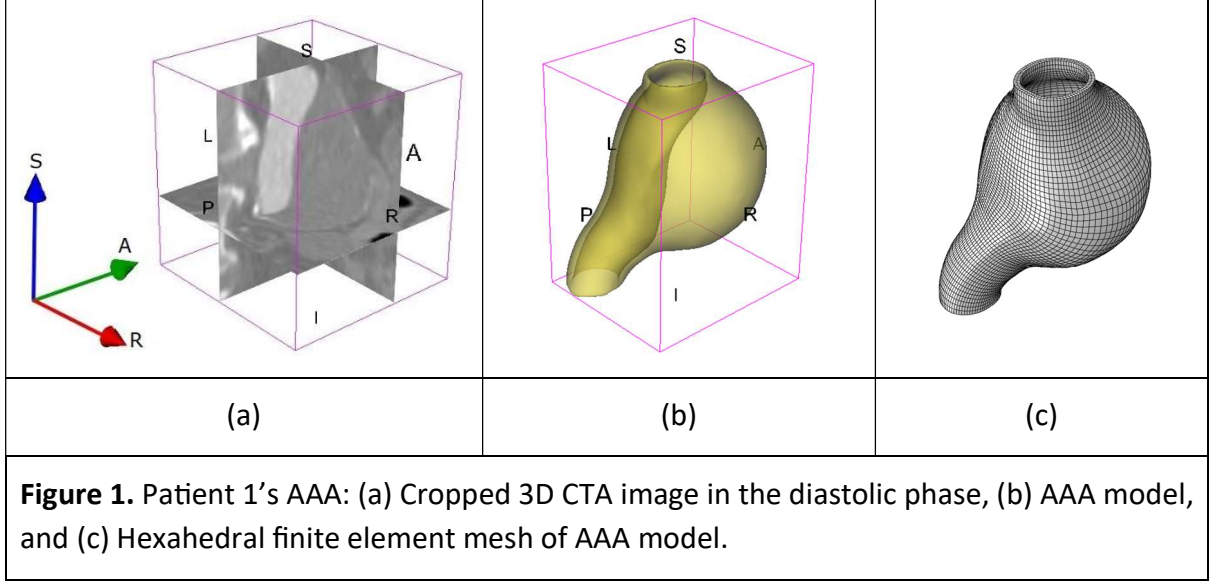
In this paper, we developed, verified, and applied to ten real AAAs, a patient-specific approach to AAA kinematic analysis using 4D CTA image data. The remainder of the paper is organized as follows: In Section 2, we presented the image data of AAA patients and the methods for estimating wall displacement and strain from registration, as well as the preparation of synthetic ground truth image data. In Section 3, We verified our approach against synthetic ground truth. In Section 4, we presented AAA wall displacements and strains in ten patients, followed by our conclusions and discussions in Section 5.

2. Materials and methods

2.1. Image data

We used anonymized contrast-enhanced 4D CTA image data sets of ten patients diagnosed with AAA. Patients were recruited at Fiona Stanley Hospital (Western Australia, Australia) and provided their informed consent prior to their involvement in the research. The study was conducted in accordance with the Declaration of Helsinki, and the protocol was approved by Human Research Ethics and Governance at South Metropolitan Health Service (HREC-SMHS) (approval code RGS3501), and by Human Research Ethics Office at The University of Western Australia (approval code RA/4/20/5913).

As an example, Figure 1a shows the cropped 3D CTA image of Patient 1's AAA in the diastolic phase. This image has dimensions of (112, 109, 74) voxels and voxel spacing of (0.627, 0.627, 1.000) mm along (R, A, S) axes, as illustrated in Figure 1a. In the patient coordinate system, the basis is aligned with the anatomical axes of anterior-posterior, inferior-superior, and left-right. Specifically, the axes R, A, and S correspond, respectively, to left-right, posterior-anterior, and inferior-superior directions.



2.2. Image registration, displacement, and strain

In this study, we used deformable image registration to align systolic and diastolic 3D frames of 4D CTA and estimate the displacement field that maps systolic to diastolic AAA geometry. We then extracted wall displacements from the registration displacement map and subsequently computed strain.

Regularized image registration theory: We used MATLAB implementation of a deformable image registration with isotropic total variation regularization of displacement (Vishnevskiy, Gass et al. 2017). The regularized image registration, within a discretized image domain Ω , estimates the three-dimensional displacement field $\mathbf{d} : \Omega \rightarrow \mathbb{R}^3$ that maps a moving image \mathbf{I}_M onto a fixed image \mathbf{I}_F via the following optimization problem:

$$\mathbf{d}^* = \underset{\mathbf{d}}{\operatorname{argmin}} \mathcal{F}(\mathbf{d}) = \underset{\mathbf{d}}{\operatorname{argmin}} E_D(\mathbf{d}; \mathbf{I}_F, \mathbf{I}_M) + \lambda E_R(\mathbf{d}), \quad (1)$$

where E_D is an image dissimilarity metric and E_R is the displacement regularization term with coefficient λ controlling the amount of regularization. The fixed and moving images are composed of $L = |\Omega|$ voxels. Each voxel has the physical dimensions $(\delta_1, \delta_2, \delta_3)$ along directions $(1, 2, 3)$ and the volume $v = \delta_1 \delta_2 \delta_3$.

For subsequent analysis, we treated the images and the displacement components fields as vectors i.e., $\mathbf{I} \in \mathbb{R}^L$ and $\mathbf{d}_i \in \mathbb{R}^L$ for $i = 1, 2, 3$ with \mathbf{d}_i being the i th component of the displacement field $\mathbf{d} = (\mathbf{d}_1^T, \mathbf{d}_2^T, \mathbf{d}_3^T)^T \in \mathbb{R}^{L \times 3}$.

To reduce the dimensionality of search space in the optimization problem (Eq. 1), we parametrized the displacement field \mathbf{d} by interpolating the displacement field \mathbf{k} on a structured and evenly spaced grid of M control points i.e., $\mathbf{d} = \mathbf{d}(\mathbf{k})$. The control point grid spacing is (K_1, K_2, K_3) voxels or in physical dimensions $(\delta_1 K_1, \delta_2 K_2, \delta_3 K_3)$, along directions $(1, 2, 3)$. Then, the cell volume of the control point grid is $\eta = v K_1 K_2 K_3 = \delta_1 \delta_2 \delta_3 K_1 K_2 K_3$.

For subsequent analysis, we treated the displacement components of control points as vectors i.e., $\mathbf{k}_i \in \mathbb{R}^M$ for $i = 1, 2, 3$ with \mathbf{k}_i being the i th component of the control points displacement field $\mathbf{k} = (\mathbf{k}_1^\top, \mathbf{k}_2^\top, \mathbf{k}_3^\top)^\top \in \mathbb{R}^{M \times 3}$.

While cubic B-splines are more common in deformable image registration, in this study, we used first-order B-splines with smaller spatial support to ensure that the interpolated displacements are bounded by the control point displacements and to eliminate overshooting effects when approximating sharp image gradients, such as those in the AAA wall region.

As a smooth image dissimilarity metric, we employed the local correlation coefficient (LCC) between the two images \mathbf{I}_F and \mathbf{I}_M defined as (Cachier and Pennec 2000):

$\text{LCC}(\mathbf{I}_F, \mathbf{I}_M) = - \sum_{\mathbf{x} \in \Omega} \frac{\mathbf{I}_F \circ \overline{\mathbf{I}_M} - \overline{\mathbf{I}_F} \circ \overline{\mathbf{I}_M}}{\sqrt{\mathbf{I}_F^2 - \overline{\mathbf{I}_F}^2} \circ \sqrt{\mathbf{I}_M^2 - \overline{\mathbf{I}_M}^2}} [\mathbf{x}] v, \quad (2)$	
--	--

with \circ denoting the elementwise multiplication operator. The image average $\overline{\mathbf{I}} = H_w \otimes \mathbf{I}$ is calculated by convolutions using a Gaussian weighting kernel H_w with standard bandwidth w , with \otimes denoting the convolution operator. Also, the operator $\mathbf{I}[\mathbf{x}]$ interpolates the image \mathbf{I} at position \mathbf{x} .

We imposed total variation regularization on the control point displacement field \mathbf{k} rather than the dense voxel displacement field \mathbf{d} , as follows:

$E_R^{TV}(\mathbf{k}) = \eta \sum_{m \leq M} \sqrt{\sum_{i,j \leq 3} (\nabla_i k_j[m])^2}, \quad (3)$	
---	--

where ∇_i denotes the derivative operator along the i th direction, and $k_j[m]$ for $j = 1, 2, 3$ denotes the j th component of the control point displacement field at the control point index m . Hence, $\mathbf{k}[m] = (k_1[m], k_2[m], k_3[m])^\top \in \mathbb{R}^3$ represents the displacement vector of the m th control point. Total variation regularization is more effective in estimating displacements that do not align with the Cartesian coordinate axes (Vishnevskiy, Gass et al. 2017).

Finally, we reformulated the optimization problem for the total variation-regularized image registration in terms of the control point displacement field, as follows:

$$\mathbf{k}^* = \underset{\mathbf{k}}{\operatorname{argmin}} \mathcal{F}(\mathbf{d}(\mathbf{k})) = \underset{\mathbf{d}}{\operatorname{argmin}} E_D(\mathbf{d}(\mathbf{k}); \mathbf{I}_F, \mathbf{I}_M) + \lambda E_R^{TV}(\mathbf{k}). \quad (4)$$

Wall displacement: Registering the undeformed image onto the deformed image yielded the control point displacement field \mathbf{k} that was then interpolated at the AAA wall location to obtain the wall displacement from registration in the Cartesian patient coordinate system (R, A, S).

Registration is known to produce more accurate displacements in the direction of image gradients (Lehoucq, Reu et al. 2021). For AAA 3D CTA images, the image gradient in the wall region mostly aligns with the wall normal. Therefore, for subsequent analysis, we established a local biological coordinate system comprising the local normal and the local tangent to the wall surface.

To extract a smooth field of unit normal vectors on the AAA surface, we employed the planar least squares regression method in which the normal at each point in the point cloud is determined by fitting a local plane using neighbouring points. For AAA, the point cloud consists of the STL vertices on the external surface of the AAA wall model.

In first-order 3D plane fitting (Berkmann and Caelli 1994), finding the surface normal at a query point is simplified by estimating the normal of a tangent plane through a least-square plane fitting approach (Shakarji 1998). The solution for estimating the surface normal is therefore reduced to the Principal Component Analysis (PCA) of a covariance matrix created from the nearest neighbours of the query point. Once the neighbouring points set \mathcal{P}^k of a given query point \mathbf{p} in the point cloud are identified, the covariance matrix \mathbf{C} for the query point \mathbf{p} is assembled as

$$\mathbf{C} = \frac{1}{k} \sum_{i=1}^k (\mathbf{p}_i - \bar{\mathbf{p}}) \otimes (\mathbf{p}_i - \bar{\mathbf{p}}), \quad (5)$$

where k is the number of neighboring points $\mathbf{p}_i \in \mathcal{P}^k$ in the vicinity of \mathbf{p} and $\bar{\mathbf{p}}$ represents the centroid of these neighboring points. Matrix \mathbf{C} is symmetric and positive semi-definite with real eigenvalues λ_j for $j = 1, 2, 3$. The corresponding eigenvectors \mathbf{v}_j form an orthogonal

basis, corresponding to the principal components of \mathcal{P}^k . If $0 \leq \lambda_1 \leq \lambda_2 \leq \lambda_3$, the eigenvector \mathbf{v}_1 corresponding to the smallest eigenvalue λ_1 is the normal. Figure 2 illustrates the unit normal vectors on AAA surface, obtained via planar regression, which is a smooth vector field suitable for defining biological coordinates.

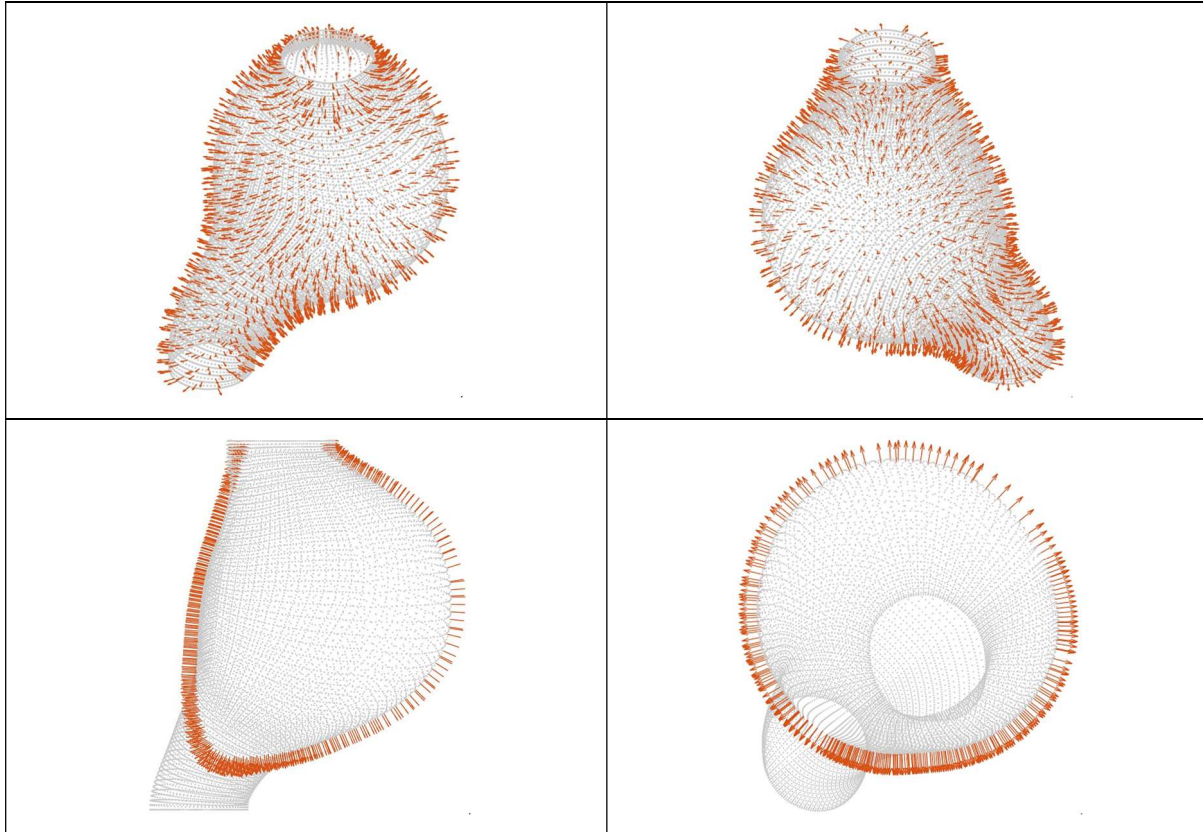


Figure 2. Smooth field of unit normal vectors on AAA surface using planar regression

Wall strain: As will be discussed later in Section 3, the component-wise analysis of the registration displacement field revealed that the tangential displacement from registration is an unreliable measurement. Furthermore, although the normal displacement from registration was satisfactorily estimated, it was noisy, and its spatial derivatives for strain calculation would intensify this noise. Therefore, any differential kinematic description of wall deformation must be based solely on the normal registration displacement.

(Wittek, Derwich et al. 2018) employed finite element method to compute strain field using wall motion data from 4D ultrasound and demonstrated the predominance of circumferential strain as a physiologically meaningful measurement of AAA wall strain. (Karatolios, Wittek et al. 2013) demonstrated that the mean of this circumferential strain is in good agreement with

the ratio of diameter change to diameter, which represents the circumferential strain of a uniformly inflated membrane with circular cross-section (Hencky 1915, Fichter 1997, Coelho, Roehl et al. 2014). Similarly, (Morrison, Choi et al. 2009) calculated the Green strain component in the circumferential direction as $0.5(\lambda^2 - 1)$, where λ represented the systolic to diastolic circumference ratio, equivalent to the ratio of systolic to diastolic mean diameters. Guided by (Morrison, Choi et al. 2009, Karatolios, Wittek et al. 2013), we adopted the following localized measure of circumferential wall strain:

$\epsilon = \frac{\Delta r}{r},$	(6)
----------------------------------	-----

where r is the local radius of wall curvature and Δr is the local normal displacement of the wall obtained via registration. Under the assumption that the aneurysm wall locally deforms as a uniformly expanding (with no axial stretching) homogenous cylinder made of incompressible material, our simplified measure of strain (Eq. 6) corresponds to the following Green strain tensor in the local cylindrical coordinate system composed of radial, circumferential, and axial directions, respectively:

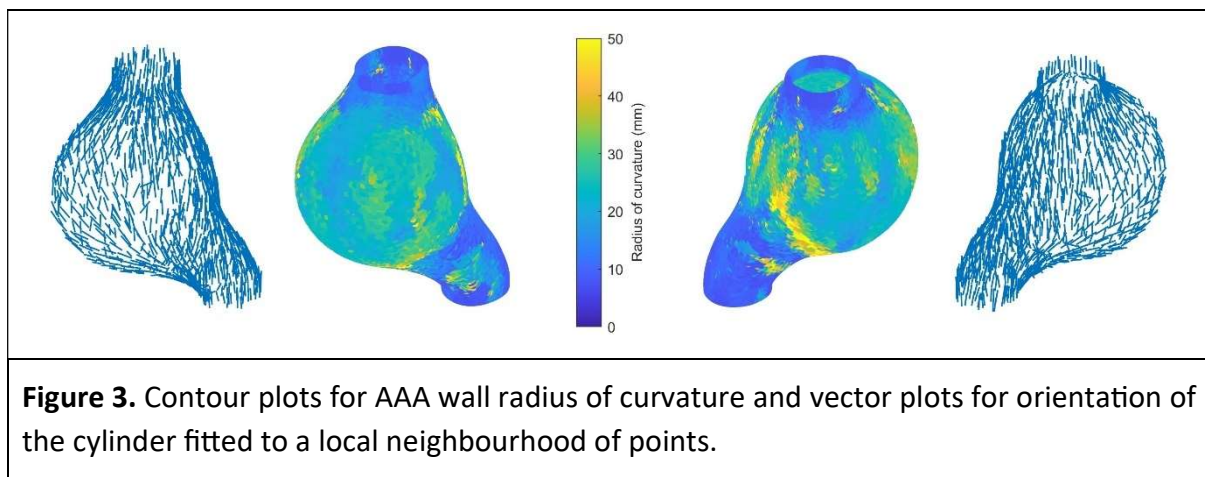
$\mathbf{E} = \begin{bmatrix} \frac{1}{2(\epsilon+1)^2} - \frac{1}{2} & 0 & 0 \\ 0 & \frac{(\epsilon+1)^2}{2} - \frac{1}{2} & 0 \\ 0 & 0 & 0 \end{bmatrix}.$	(7)
--	-----

Wall curvature: As AAA wall is represented by image-based point cloud data, traditional derivative-based methods for estimating local wall curvature cannot yield reliable results due to their high sensitivity to errors in the primitive data. On the other hand, the accuracy of least-squares methods for locally fitting a cylinder to a neighbourhood of points is diminished by outliers. Therefore, we used a variant of Random Sample Consensus (RANSAC) algorithm that identifies outliers and estimates the desired model using just inliers (Fischler and Bolles 1981).

To estimate the local radius of curvature for the wall point cloud, we utilized a variant of the RANSAC algorithm known as the M-estimator Sample Consensus (MSAC) algorithm (Torr and Zisserman 2000), available in MATLAB. We modified the native MATLAB MSAC algorithm to fit a cylinder to a local neighbourhood of points around a typical query point in the wall point cloud. We adopted the radius of the fitted cylinder as the local radius of curvature of the wall

at that query point. The local neighbourhood of points consists of the K-nearest neighbours of the query point, determined by the k-d tree based search algorithm (Muja and Lowe 2009), available in MATLAB. To achieve a reliable curvature measurement, we applied an orientation constraint to align the fitted cylinder axis with a reference orientation vector chosen as the inferior-superior or S axis for AAA (see Figure 1 for S axis definition).

Figure 3 shows the contour plots for radius of curvature for the external surface of AAA wall. The vector plots in Figure 3 illustrate that the modified MSAC algorithm effectively constrains the orientation of the fitted cylinder to align with the S axis. We verified the curvature estimation method using benchmark geometries with known distributions of radius of curvature, but these verification results are not reported here for brevity.



2.3. Synthetic ground truth

For verification of our method, we created synthetic ground truth image data by warping Patient 1's 3D CTA image using a realistic wall displacement obtained from a patient-specific finite element biomechanical model.

Biomechanical model: We segmented Patient 1's AAA image in Figure 1a, using the Segment Editor module in the 3D Slicer image computing platform (Fedorov, Beichel et al. 2012, Slicer 2024), to extract the voxelated geometries of AAA wall and blood. We used these geometries and the assumed wall thickness of 1.5 mm (Raut, Jana et al. 2013) as input for the BioPARR (Biomechanics-based Prediction of Aneurysm Rupture Risk) software package (Joldes, Miller et al. 2017, Joldes 2024) to automatically create AAA model, as shown in Figure 1b. We used hexahedral elements to mesh the model in HyperMesh (Alkhatib, Bourantas et al. 2023, Altair

2024). We imported the mesh into the Abaqus finite element software (Simulia 2024). The mesh, shown in Figure 1c, consists of 49530 nodes and 8892 20-node quadratic hexahedral elements with hybrid formulation and constant pressure (element type C3D20H in Abaqus) (Alkhatib, Wittek et al. 2023). We fixed the top and bottom ends of AAA and applied a uniform pressure of 13 kPa on the inner surface of the wall. We used a hyperelastic material model for the wall tissue material, with the polynomial strain energy potential given by (Raghavan and Vorp 2000):

$$W = \alpha(I_B - 3) - \beta(I_B - 3)^2, \quad (8)$$

where I_B is the first invariant of the left Cauchy–Green or Finger deformation tensor \mathbf{B} . The material parameters $\alpha = 0.174$ MPa and $\beta = 1.881$ MPa are from the literature (Raghavan and Vorp 2000, Raghavan, Vorp et al. 2000, Fillinger, Raghavan et al. 2002, Doyle, Callanan et al. 2007). Finally, we solved Patient 1’s AAA finite element model using Abaqus/Standard solver (Simulia 2024).

Figure 4 displays the synthetic ground truth AAA wall deformation calculated using the AAA biomechanical model shown in Figure 1c. This figure highlights a non-uniform distribution of wall displacement, with a maximum of 1.37 mm.

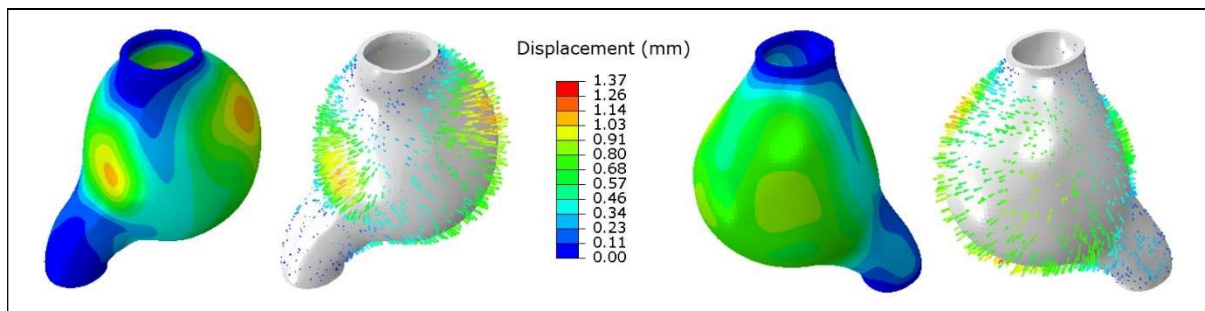


Figure 4. Contour plots of displacement magnitude and vector plots of displacement from the biomechanics-calculated AAA wall deformation used as ground truth for method verification.

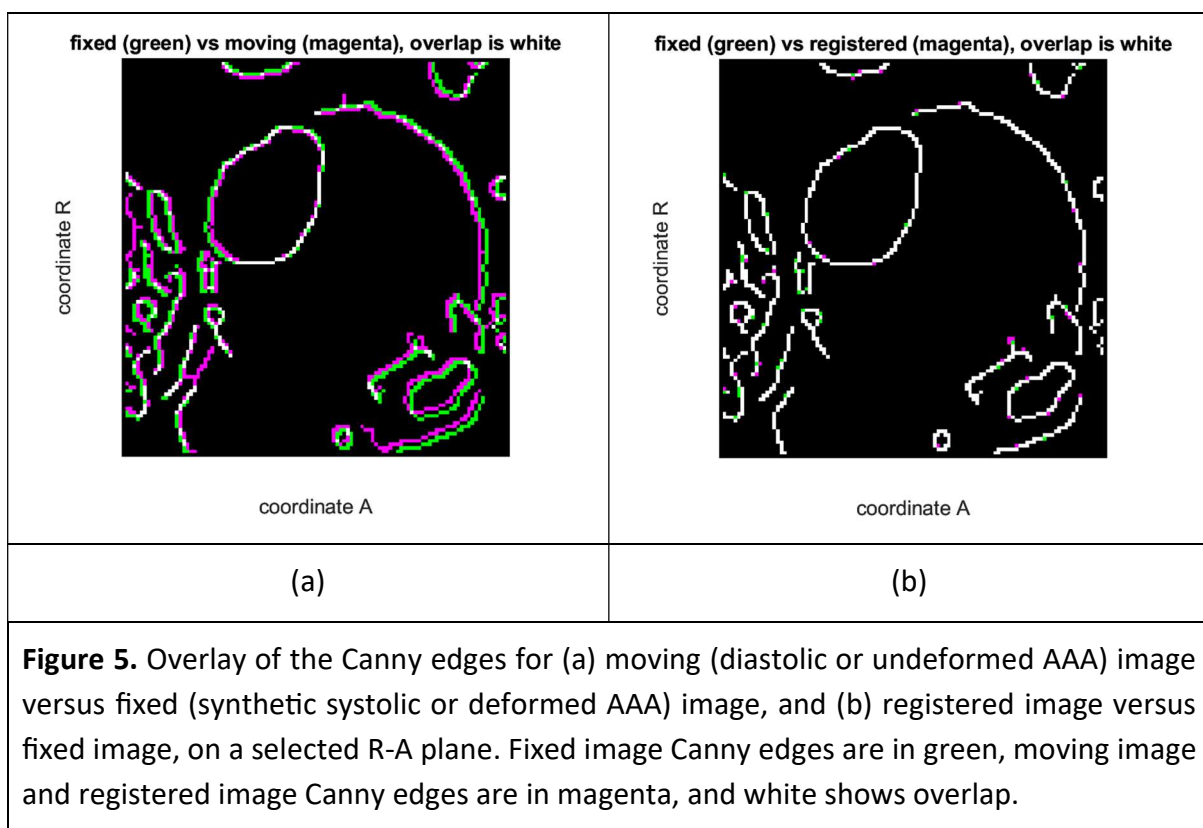
Verification approach and synthetic systolic image: We warped Patient 1’s AAA image in the diastolic phase, shown in Figure 1a, using 3D Slicer Transforms module to create the synthetic systolic image. We used the Scattered Transform Extension (Joldes 2017) in 3D Slicer to create a B-Spline warping transform based on the biomechanics-calculated AAA wall displacement as ground truth. The Scattered Transform was originally developed to warp preoperative brain

images based on a deformation field obtained from a biomechanical model (Joldes, Wittek et al. 2012).

3. Method verification

Image registration: To estimate wall displacement from registration, we employed Patient 1's diastolic (undeformed) and synthetic systolic (deformed) images as the moving and fixed images, respectively, in deformable image registration. We set the control points spacing $(K_1, K_2, K_3) = (6, 6, 6)$ voxels, and the regularization coefficient $\lambda = 0.05$.

Figure 5 compares the moving versus fixed and the registered versus fixed images by their Canny edge overlays (Canny 1986). While the Canny edge overlays demonstrate a good match between the fixed and registered images, we carefully examined the registration displacement field, as follows, before strain calculation.

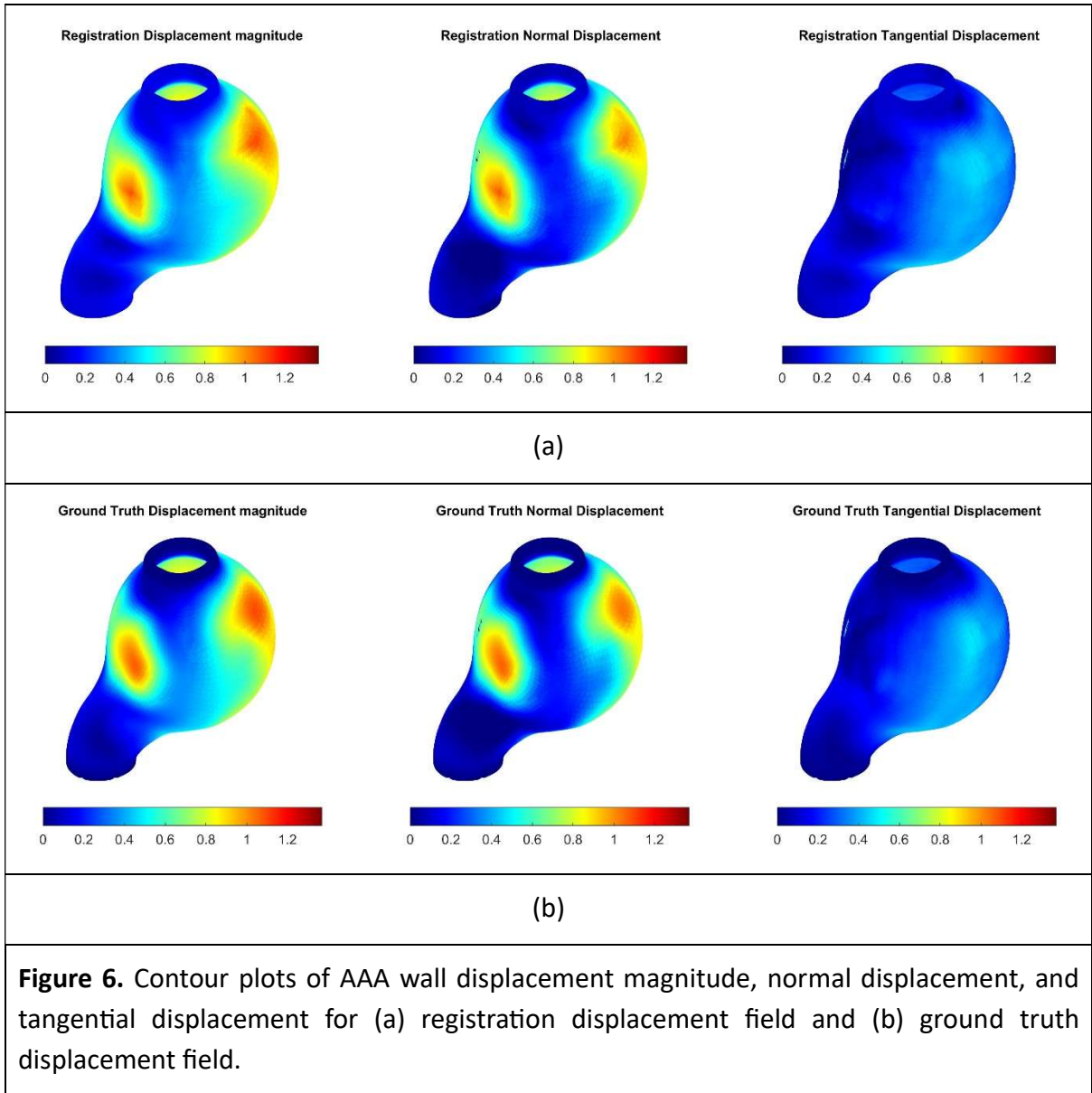


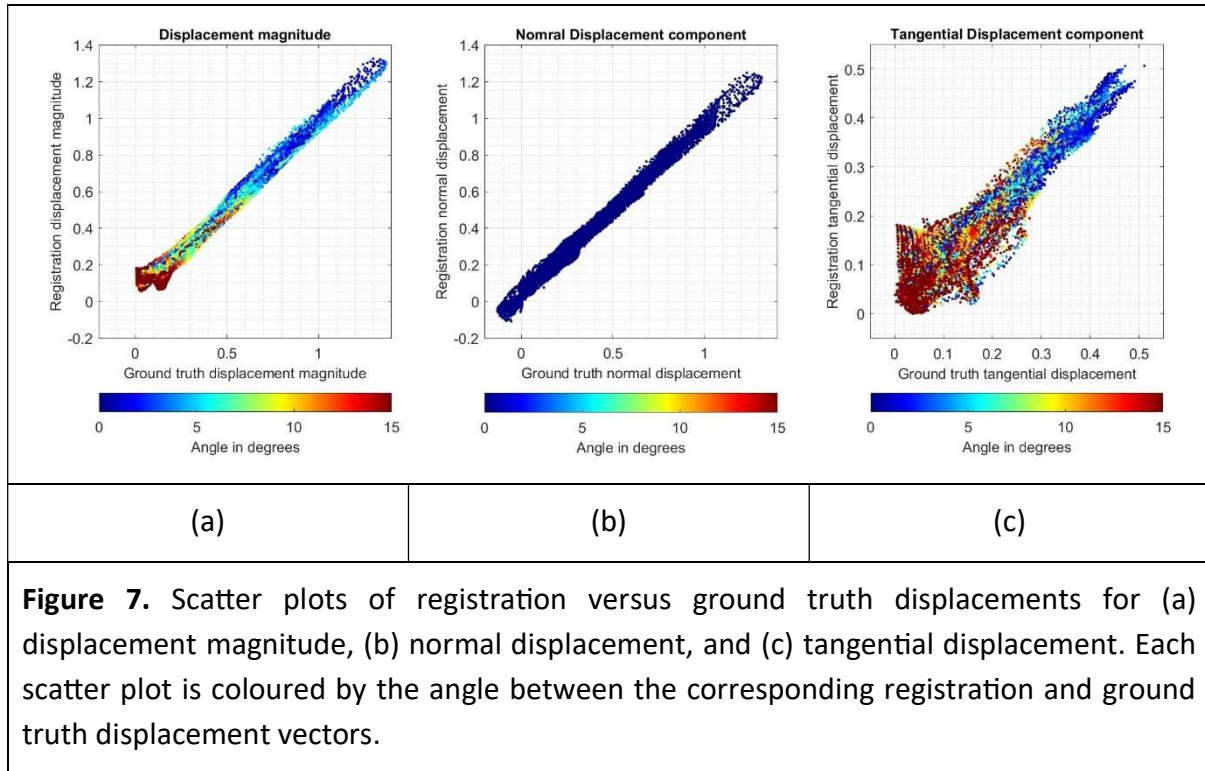
Wall displacement: With the local biological coordinates established, as described in Section 2.2, we decomposed the local wall displacement vector into its normal and tangential components. Figure 6 shows the contour plots of displacement magnitude, normal displacement, and tangential displacement for both the registration and ground truth displacement fields. Figure 7 provides a closer examination of the displacements through scatter plots depicting the registration versus ground truth displacements for displacement magnitude, normal displacement, and tangential displacement.

Figure 7 shows that the normal displacement component exhibits a relatively tight scatter around the identity line, suggesting a better correspondence between registration and ground truth, when compared to the tangential displacement component. Noteworthy is that both the registration and ground truth normal displacement vectors align with the surface normal and differ only in magnitude. However, the registration and ground truth tangential displacement vectors differ in both magnitude and direction.

Figure 7 also demonstrates that the tangential displacement component displays a wide scatter around the identity line, indicating significant discrepancies between the registration and ground truth tangential displacement magnitude. Furthermore, the colour code in the tangential displacement scatter plot in Figure 7 illustrates large differences in tangential displacement direction between registration and ground truth, particularly pronounced for smaller values of tangential displacement.

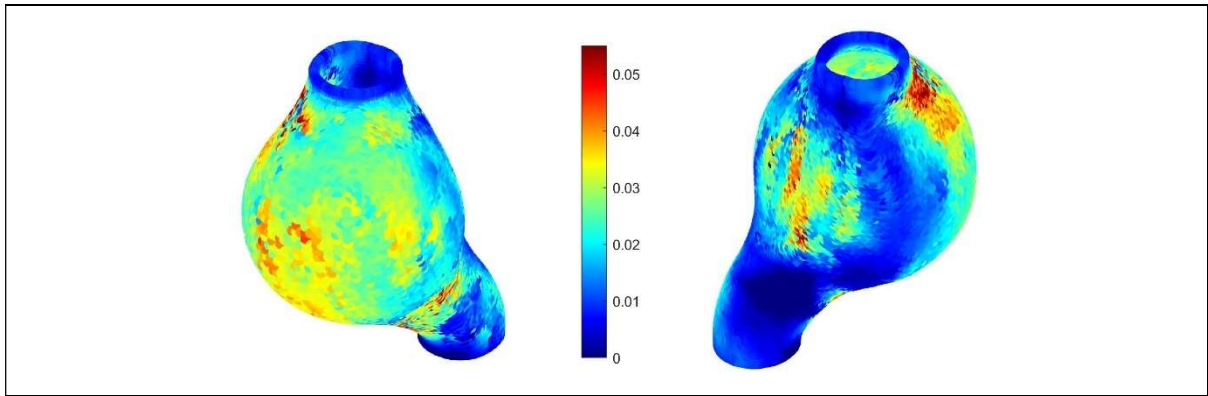
Therefore, we discarded the unreliable tangential displacement and used only the normal displacement in strain calculation. The prominence of the normal wall displacement has previously been hypothesized based on observations from fluid-structure interaction simulations (Nagy, Csobay-Novák et al. 2015).



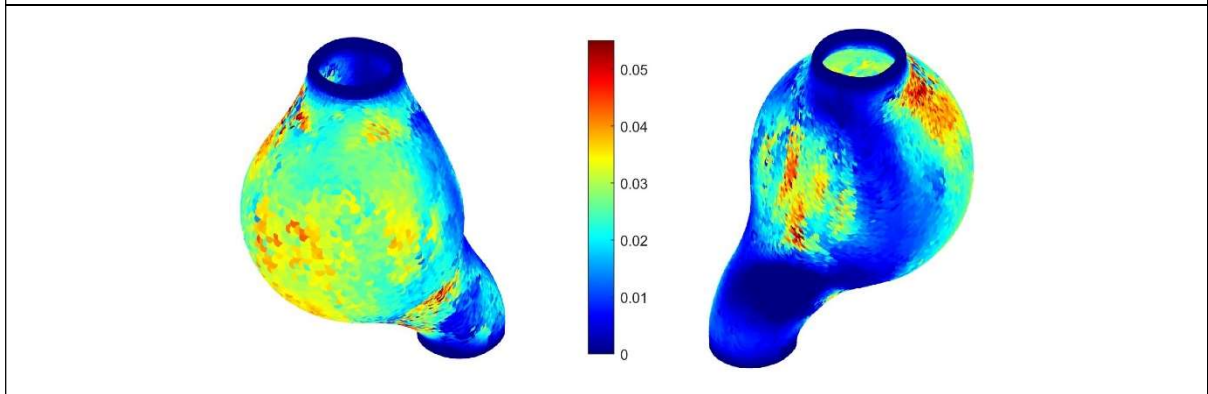


Wall strain: Figure 8 compares the wall strain obtained from registration, defined as the ratio of normal registration displacement to the local wall radius of curvature, against the ground truth wall strain. Figures 8a and 8b display the contour plots of registration and ground truth wall strain, respectively. Figure 8c offers a detailed analysis of strain verification through a scatter plot comparing the registration and ground truth strain. The relatively tight scatter in Figure 8c verifies the methods we developed for AAA kinematic analysis.

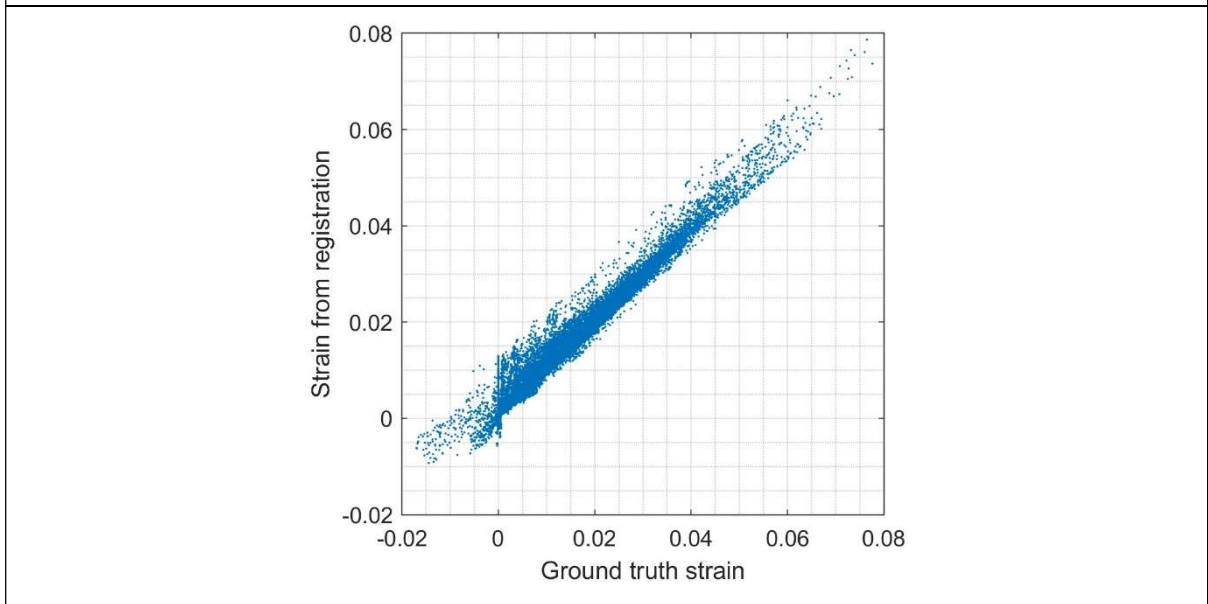
Due to the features of the methods that we used for estimating wall displacement and curvature, the wall strain may include outliers arising from large displacement outliers and small radius of curvature outliers. Therefore, following the practice used in AAA stress analysis (Speelman, Bosboom et al. 2008, Wittek, Alkhatib et al. 2022, Alkhatib, Jamshidian et al. 2024), we reported the 99th percentile of strain, rather than the peak strain. The 99th percentile of wall strain from the registration and ground truth were 5.49% and 5.36%, respectively, implying a relative difference of 2.4%. This further verifies our AAA kinematic analysis method.



(a)



(b)



(c)

Figure 8. Contour plots of (a) wall strain from registration and (b) ground truth wall strain, (c) the scatter plot of wall strain from registration versus ground truth wall strain.

4. Results

We employed our methods to assess AAA wall displacements and strains in ten patients. For each patient, we used the diastolic and systolic phases of 4D CTA image data as the moving and fixed images in deformable image registration, respectively.

Table 1 and Table 2 present AAA kinematic analysis results for our ten patients. Table 1 reports, for each patient, the AAA wall geometry, vector plots of wall displacement, contour plots of wall normal displacement, and contour plots of wall strain, using patient-specific contour limits. Table 2 reports, for each patient, the 99th percentile of wall displacement magnitude U_o , 99th percentile of wall normal displacement u_o , and 99th percentile of wall strain ϵ_o .

At first glance, the strain maps in Table 1 reveal that, in most cases, the highest strain occurs in the anterior regions of AAA wall, with the spine limiting stretching in the posterior region. In particular, comparing Patient 1's AAA strain map in Figure 8, obtained using the biomechanical model, against Patient 1's AAA actual strain map in Table 1 reveals that, according to biomechanical simulation, the wall stretches freely in both the posterior and anterior regions, while in reality, the spine restricts wall stretch in the posterior region.

Table 2 shows that, among all patients, the 99th percentile of actual wall displacement magnitude ranged from 0.75 mm to 1.40 mm, with an average of 1.14 mm and a standard deviation of 0.23 mm, while the 99th percentile of actual wall normal displacement ranged from 0.53 mm to 1.20 mm, with an average of 0.88 mm and a standard deviation of 0.20 mm. The 99th percentile of actual wall strain among all patients ranged from 3.16% to 7.31%, with an average of 5.36% and a standard deviation of 1.28%. The small ratio of standard deviation to average in these results suggest consistency in AAA kinematics across all patients.

Table 1. AAA kinematic analysis results for ten patients. For each patient, the AAA wall geometry, vector plots of wall displacement, contour plots of wall normal displacement, and contour plots of wall strain are displayed. Patient-specific contour limits, including the 99th percentile of wall displacement magnitude U_o , 99th percentile of wall normal displacement u_o , and 99th percentile of wall strain ϵ_o , are reported for each patient.

Patient number	AAA wall geometry	Wall displacement vector (mm)	Wall normal displacement (mm)	Wall strain
		$-U_o$ 0 $+U_o$ 	$-u_o$ 0 $+u_o$ 	$-\epsilon_o$ 0 $+\epsilon_o$
1		 $U_o = 1.32$ mm	 $u_o = 0.97$ mm	 $\epsilon_o = 6.73$ %
2		 $U_o = 1.31$ mm	 $u_o = 1.20$ mm	 $\epsilon_o = 7.31$ %
3		 $U_o = 0.86$ mm	 $u_o = 0.55$ mm	 $\epsilon_o = 3.16$ %
4		 $U_o = 1.20$ mm	 $u_o = 0.94$ mm	 $\epsilon_o = 5.15$ %

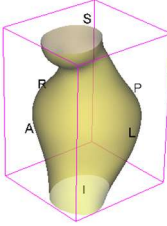
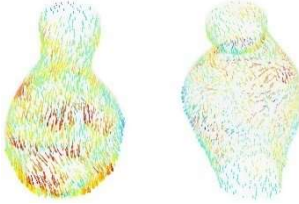
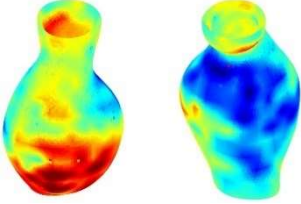
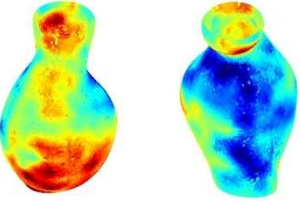
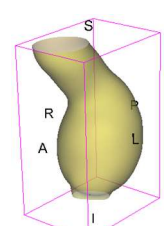

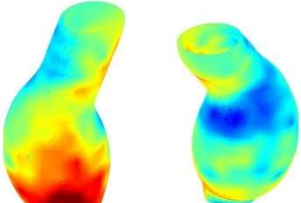
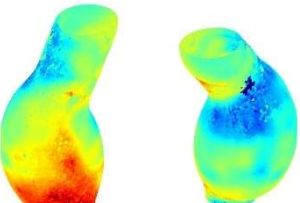
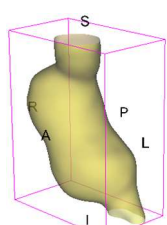
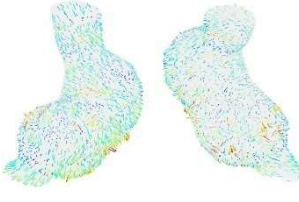
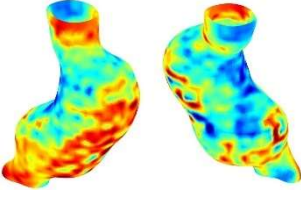
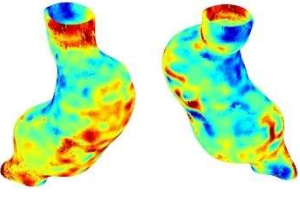
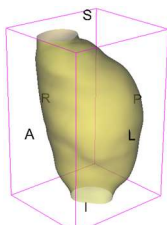
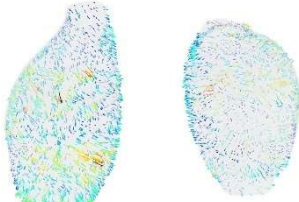
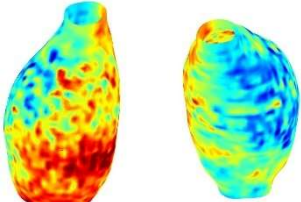
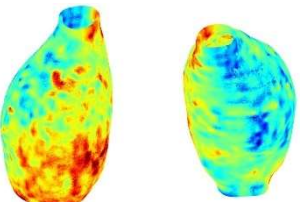
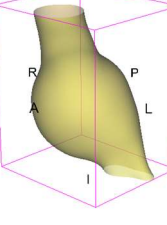
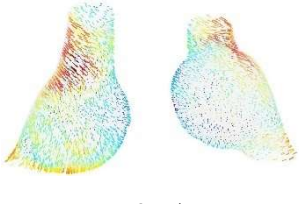
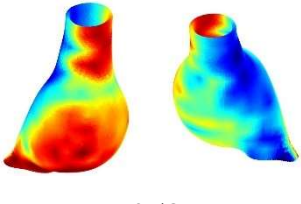
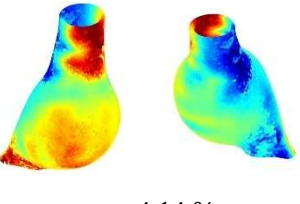
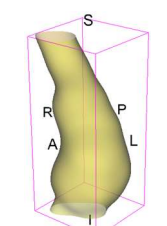

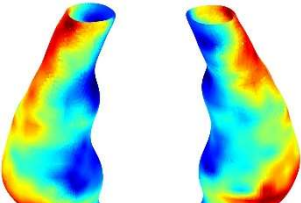
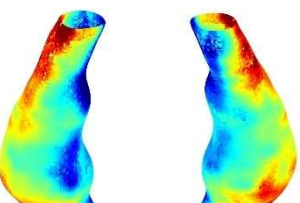
5		 <p>$U_o = 1.13 \text{ mm}$</p>	 <p>$u_o = 0.91 \text{ mm}$</p>	 <p>$\epsilon_o = 4.12 \%$</p>
6		 <p>$U_o = 0.99 \text{ mm}$</p>	 <p>$u_o = 0.93 \text{ mm}$</p>	 <p>$\epsilon_o = 5.21 \%$</p>
7		 <p>$U_o = 1.40 \text{ mm}$</p>	 <p>$u_o = 1.03 \text{ mm}$</p>	 <p>$\epsilon_o = 6.18 \%$</p>
8		 <p>$U_o = 1.02 \text{ mm}$</p>	 <p>$u_o = 0.80 \text{ mm}$</p>	 <p>$\epsilon_o = 5.53 \%$</p>
9		 <p>$U_o = 0.75 \text{ mm}$</p>	 <p>$u_o = 0.53 \text{ mm}$</p>	 <p>$\epsilon_o = 4.14 \%$</p>
10		 <p>$U_o = 1.39 \text{ mm}$</p>	 <p>$u_o = 0.92 \text{ mm}$</p>	 <p>$\epsilon_o = 6.07 \%$</p>

Table 2. AAA kinematic analysis results for ten patients. For each patient, the 99th percentile of wall displacement magnitude U_o , 99th percentile of wall normal displacement u_o , and 99th percentile of wall strain ϵ_o , are reported.

Patient number	U_o (mm)	u_o (mm)	ϵ_o (%)
1	1.32	0.97	6.73
2	1.31	1.20	7.31
3	0.86	0.55	3.16
4	1.20	0.94	5.15
5	1.13	0.91	4.12
6	0.99	0.93	5.21
7	1.40	1.03	6.18
8	1.02	0.80	5.53
9	0.75	0.53	4.14
10	1.39	0.92	6.07
Minimum	0.75	0.53	3.16
Maximum	1.40	1.20	7.31
Average	1.14	0.88	5.36
Standard deviation	0.23	0.20	1.28

5. Conclusions and discussions

We developed an image registration-based approach for patient-specific AAA kinematic analysis, enabling non-invasive, in-vivo measurement of AAA wall displacements and strains from time-resolved 3D computed tomography angiography (4D CTA) images.

We estimated the wall displacement by registering the diastolic phase image of 4D CTA image data (moving image), onto the systolic phase image (fixed image). We used deformable image registration with isotropic total variation regularization of displacement. Using planar regression and Principal Component Analysis, we established local biological coordinate systems, including local normal and tangential directions to AAA wall, and decomposed the local wall displacement into its normal and tangential components. The component-wise analysis of the wall registration displacement indicated that the tangential displacement

component was unreliable, whereas the normal wall displacement was satisfactorily estimated and hence used for strain calculation.

We calculated the local AAA wall strain as the ratio of displacement normal to the wall to its local radius of curvature, with clear interpretation in terms of Green strain components. We estimated the local radius of wall curvature using local cylinder fitting with a Random Sample Consensus (RANSAC) algorithm.

We verified our approach by demonstrating an excellent match between the registration and biomechanically established ground truth wall displacements and strains.

We assessed wall displacements and strain in ten patients. Among all patients, the 99th percentile of circumferential wall strain ranged from 3.16% to 7.31%, with an average of 5.36% and a standard deviation of 1.28%. Noteworthy was that the spine restricted AAA stretching in the posterior region.

Nevertheless, limitations of our method need to be clearly articulated. In current clinical practice of AAA diagnosis and treatment, 4D CTA is not used. However, it is a common imaging modality in cardiology and therefore easily translatable to vascular disease management.

As image gradients in direction tangential to AAA wall are small, our image registration method is unable to capture reliably the tangential components of AAA wall displacements. Therefore, in strain estimation we must rely only on the normal component of the displacement vector and not on all three displacement vector components. This clearly inhibits the ability to identify a full finite strain tensor.

Despite these limitations, our approach offers the clear advantage of evaluating aneurysm displacements and strains locally, allowing for point-by-point evaluation.

Acknowledgements

This work was supported by the Australian National Health and Medical Research Council NHMRC Ideas grant no. APP2001689. The authors acknowledge the contributions of Christopher Wood and Jane Polce, radiology technicians at the Medical Imaging Department, Fiona Stanley Hospital (Murdoch, Western Australia), to patient image acquisition.

References

- Alkhatib, F., G. C. Bourantas, A. Wittek and K. Miller (2023). Generation of Patient-specific Structured Hexahedral Mesh of Aortic Aneurysm Wall. Computational Biomechanics for Medicine - Towards Automation and Robustness of Computations in the Clinic. M. P. Nash, A. Wittek, P. M. F. Nielsen et al. Singapore, Springer International Publishing: 3-21.
- Alkhatib, F., M. Jamshidian, D. Le Liepvre, F. Bernard, L. Minvielle, A. Wittek and K. Miller (2024). "Towards Full Automation of Geometry Extraction for Biomechanical Analysis of Abdominal Aortic Aneurysm; Neural Network-Based versus Classical Methodologies." arXiv.
- Alkhatib, F., A. Wittek, B. F. Zwick, G. C. Bourantas and K. Miller (2023). "Computation for biomechanical analysis of aortic aneurysms: the importance of computational grid." Computer Methods in Biomechanics and Biomedical Engineering: 1-17.
- Altair. (2024). "HyperMesh." from <https://altair.com/hypermesh>.
- Berkmann, J. and T. Caelli (1994). "Computation of Surface Geometry and Segmentation Using Covariance Techniques." IEEE Transactions on Pattern Analysis and Machine Intelligence **16**(11): 1114-1116.
- Cachier, P. and X. Pennec (2000). "3D non-rigid registration by gradient descent on a Gaussian-windowed similarity measure using convolutions." IEEE Workshop on Mathematical Methods in Biomedical Image Analysis, Proceedings: 182-189.
- Canny, J. (1986). "A computational approach to edge detection." IEEE Transactions on pattern analysis and machine intelligence **6**: 679-698.
- Cebull, H. L., A. H. Soepriatna, J. J. Boyle, S. M. Rothenberger and C. J. Goergen (2019). "Strain Mapping From Four-Dimensional Ultrasound Reveals Complex Remodeling in Dissecting Murine Abdominal Aortic Aneurysms." Journal of Biomechanical Engineering-Transactions of the Asme **141**(6): 060907.
- Chung, T. K., N. L. Liang and D. A. Vorp (2022). "Artificial intelligence framework to predict wall stress in abdominal aortic aneurysm." Applications in Engineering Science **10**: 100104.
- Coelho, M., D. Roehl and K. U. Bletzinger (2014). "Numerical and analytical solutions with finite strains for circular inflated membranes considering pressure-volume coupling." International Journal of Mechanical Sciences **82**: 122-130.
- Darling, R., C. Messina, D. Brewster and L. Ottinger (1977). "Autopsy Study of Unoperated Abdominal Aortic Aneurysms. The Case for Early Resection." Circulation **56**(3 Suppl): II161-164.
- Derwich, W., T. Keller, N. Filmann, T. Schmitz-Rixen, C. Blasé, K. Oikonomou and A. Wittek (2023). "Changes in Aortic Diameter and Wall Strain in Progressing Abdominal Aortic Aneurysms." Journal of Ultrasound in Medicine **42**(8): 1737-1746.
- Doyle, B. J., A. Callanan and T. M. McGloughlin (2007). "A comparison of modelling techniques for computing wall stress in abdominal aortic aneurysms." Biomedical Engineering Online **6**: 1-12.
- Farotto, D., P. Segers, B. Meuris, J. V. Sloten and N. Famaey (2018). "The role of biomechanics in aortic aneurysm management: requirements, open problems and future prospects." Journal of the Mechanical Behavior of Biomedical Materials **77**: 295-307.

Fedorov, A., R. Beichel, J. Kalpathy-Cramer, J. Finet, J.-C. Fillion-Robin, S. Pujol, C. Bauer, D. Jennings, F. Fennessy, M. Sonka, J. Buatti, S. Aylward, J. V. Miller, S. Pieper and R. Kikinis (2012). "3D Slicer as an Image Computing Platform for the Quantitative Imaging Network." Magnetic Resonance Imaging **30**(9): 1323-1341.

Fichter, W. B. (1997). "Some solutions for the large deflections of uniformly loaded circular membranes (NASA Technical Paper 3658)." from <https://ntrs.nasa.gov/citations/19970023537>.

Fillinger, M. F., S. P. Marra, M. L. Raghavan and F. E. Kennedy (2003). "Prediction of Rupture Risk in Abdominal Aortic Aneurysm during Observation: Wall Stress versus Diameter." Journal of Vascular Surgery **37**(4): 724-732.

Fillinger, M. F., M. L. Raghavan, S. P. Marra, J. L. Cronenwett and F. E. Kennedy (2002). "In vivo Analysis of Mechanical Wall Stress and Abdominal Aortic Aneurysm Rupture Risk." Journal of Vascular Surgery **36**(3): 589-597.

Fischler, M. A. and R. C. Bolles (1981). "Random Sample Consensus - a Paradigm for Model-Fitting with Applications to Image-Analysis and Automated Cartography." Communications of the ACM **24**(6): 381-395.

Gasser, T. C., M. Auer, F. Labruto, J. Swedenborg and J. Roy (2010). "Biomechanical Rupture Risk Assessment of Abdominal Aortic Aneurysms: Model Complexity versus Predictability of Finite Element Simulations." European Journal of Vascular and Endovascular Surgery **40**(2): 176-185.

Gasser, T. C., C. Miller, S. Polzer and J. Roy (2022). "A quarter of a century biomechanical rupture risk assessment of abdominal aortic aneurysms. Achievements, clinical relevance, and ongoing developments." International Journal for Numerical Methods in Biomedical Engineering **39**(4): e3587.

Hencky, H. (1915). "Über den Spannungszustand in kreisrunden Platten mit verschwindender Biegesteifigkeit." Zeitschrift Für Mathematik und Physik **63**: 311-317.

Indrakusuma, R., H. Jalalzadeh, R. N. Planken, H. A. Marquering, D. A. Legemate, M. J. W. Koelemay and R. Balm (2016). "Biomechanical Imaging Markers as Predictors of Abdominal Aortic Aneurysm Growth or Rupture: A Systematic Review." European Journal of Vascular and Endovascular Surgery **52**(4): 475-486.

Joldes, G. R. (2017). "Documentation/Nightly/Extensions/ScatteredTransform." Slicer Wiki Retrieved 08/05/2024, from <https://www.slicer.org/w/index.php?title=Documentation/Nightly/Extensions/ScatteredTransform&oldid=50094>.

Joldes, G. R. (2024). "BioPARR - Biomechanics based Prediction of Aneurysm Rupture Risk." from <https://bioparr.mech.uwa.edu.au/>.

Joldes, G. R., K. Miller, A. Wittek and B. Doyle (2016). "A simple, effective and clinically applicable method to compute abdominal aortic aneurysm wall stress." Journal of the Mechanical Behavior of Biomedical Materials **58**: 139-148.

Joldes, G. R., K. Miller, A. Wittek, R. O. Forsythe, D. E. Newby and B. J. Doyle (2017). "BioPARR: A software system for estimating the rupture potential index for abdominal aortic aneurysms." Scientific Reports **7**(1): 4641.

Joldes, G. R., A. Wittek, S. K. Warfield and K. Miller (2012). "Performing Brain Image Warping Using the Deformation Field Predicted by a Biomechanical Model." Computational Biomechanics for Medicine: Deformation and Flow: 89-96.

Karatolios, K., A. Wittek, T. H. Nwe, P. Bihari, A. Shelke, D. Josef, T. Schmitz-Rixen, J. Geks, B. Maisch, C. Blase, R. Moosdorf and S. Vogt (2013). "Method for Aortic Wall Strain Measurement With Three-Dimensional Ultrasound Speckle Tracking and Fitted Finite Element Analysis." Annals of Thoracic Surgery **96**(5): 1664-1671.

Kontopodis, N., D. Pantidis, A. Dedes, N. Daskalakis and C. V. Ioannou (2016). "The - Not So - Solid 5.5 cm Threshold for Abdominal Aortic Aneurysm Repair: Facts, Misinterpretations, and Future Directions." Frontiers in Surgery **3**: 1.

Lehoucq, R. B., P. L. Reu and D. Z. Turner (2021). "The Effect of the Ill-posed Problem on Quantitative Error Assessment in Digital Image Correlation." Experimental Mechanics **61**(3): 609-621.

Li, Z. Y., J. U-Ying-Im, T. Y. Tang, E. Soh, T. C. See and J. H. Gillard (2008). "Impact of calcification and intraluminal thrombus on the computed wall stresses of abdominal aortic aneurysm." Journal of Vascular Surgery **47**(5): 928-935.

Miller, K., H. Mufty, A. Catlin, C. Rogers, B. Saunders, R. Sciarrone, I. Fourneau, B. Meuris, A. Tavner, G. R. Joldes and A. Wittek (2020). "Is There a Relationship Between Stress in Walls of Abdominal Aortic Aneurysm and Symptoms?" Journal of Surgical Research **252**: 37-46.

Morrison, T. M., G. Choi, C. K. Zarins and C. A. Taylor (2009). "Circumferential and longitudinal cyclic strain of the human thoracic aorta: age-related changes." Journal of Vascular Surgery **49**(4): 1029-1036.

Muja, M. and D. G. Lowe (2009). "Fast Approximate Nearest Neighbors with Automatic Algorithm Configuration." VISAPP 2009: Proceedings of the Fourth International Conference on Computer Vision Theory and Applications **1**: 331-340.

Nagy, R., C. Csobay-Novák, A. Lovas, P. Sótonyi and I. Bojtár (2015). "Non-invasive time-dependent strain measurement method in human abdominal aortic aneurysms: Towards a novel approach to rupture risk estimation." Journal of Biomechanics **48**(10): 1876-1886.

NICE (National Institute for Health and Care Excellence). (2020). "Abdominal Aortic Aneurysm: Diagnosis and Management (NICE guideline NG156)." from www.nice.org.uk/guidance/ng156

Polzer, S., T. C. Gasser, R. Vlachovsky, L. Kubíček, L. Lambert, V. Man, K. Novák, M. Slazansky, J. Bursa and R. Staffa (2020). "Biomechanical indices are more sensitive than diameter in predicting rupture of asymptomatic abdominal aortic aneurysms." Journal of Vascular Surgery **71**(2): 617-626.

Raghavan, M. L. and D. A. Vorp (2000). "Toward a biomechanical tool to evaluate rupture potential of abdominal aortic aneurysm: identification of a finite strain constitutive model and evaluation of its applicability." Journal of Biomechanics **33**(4): 475-482.

Raghavan, M. L., D. A. Vorp, M. P. Federle, M. S. Makaroun and M. W. Webster (2000). "Wall stress distribution on three-dimensionally reconstructed models of human abdominal aortic aneurysm." Journal of Vascular Surgery **31**(4): 760-769.

Raut, S. S., A. Jana, V. De Oliveira, S. C. Muluk and E. A. Finol (2013). "The Importance of Patient-Specific Regionally Varying Wall Thickness in Abdominal Aortic Aneurysm Biomechanics." Journal of Biomechanical Engineering **135**(8): 081010.

Raut, S. S., A. Jana, S. C. Muluk, M. Doyle, R. W. Biederman and E. A. Finol (2014). "Estimation of Patient-Specific 3d in Vivo Abdominal Aortic Aneurysm Strain." Proceedings of the ASME Summer Bioengineering Conference - 2013, Pt B.

Satriano, A., S. Rivolo, G. Martufi, E. A. Finol and E. S. Di Martino (2015). "In vivo strain assessment of the abdominal aortic aneurysm." Journal of Biomechanics **48**(2): 354-360.

Shakarji, C. M. (1998). "Least-squares fitting algorithms of the NIST algorithm testing system." Journal of Research of the National Institute of Standards and Technology **103**(6): 633-641.

Simulia. (2024). "Abaqus: Finite Element Analysis for Mechanical Engineering and Civil Engineering." from <https://www.3ds.com/products/simulia/abaqus>.

Singh, T. P., J. V. Moxon, T. C. Gasser, J. Jenkins, M. Bourke, B. Bourke and J. Gollidge (2023). "Association between aortic peak wall stress and rupture index with abdominal aortic aneurysm-related events." European Radiology **33**(8): 5698-5706.

Slicer. (2024). "3D Slicer image computing platform." from <https://www.slicer.org/>.

Speelman, L., A. Bohra, E. M. H. Bosboom, G. W. H. Schurink, F. N. van de Vosse, M. S. Makaorun and D. A. Vorp (2007). "Effects of wall calcifications in patient-specific wall stress analyses of abdominal aortic aneurysms." Journal of Biomechanical Engineering-Transactions of the Asme **129**(1): 105-109.

Speelman, L., E. M. H. Bosboom, G. W. H. Schurink, F. A. M. V. I. Hellenthal, J. Buth, M. Breeuwer, M. J. Jacobs and F. N. van de Vosse (2008). "Patient-Specific AAA Wall Stress Analysis: 99-Percentile Versus Peak Stress." European Journal of Vascular and Endovascular Surgery **36**(6): 668-676.

Torr, P. H. S. and A. Zisserman (2000). "MLE-SAC: A new robust estimator with application to estimating image geometry." Computer Vision and Image Understanding **78**(1): 138-156.

Vande Geest, J., E. Di Martino, A. Bohra, M. S. Makaroun and D. A. Vorp (2006). "A Biomechanics-Based Rupture Potential Index for Abdominal Aortic Aneurysm Risk Assessment: Demonstrative Application." Annals of the New York Academy of Sciences **1085**: 11-21.

Vishnevskiy, V., T. Gass, G. Szekely, C. Tanner and O. Goksel (2017). "Isotropic Total Variation Regularization of Displacements in Parametric Image Registration." IEEE Transactions on Medical Imaging **36**(2): 385-395.

Vorp, D. A. (2007). "Biomechanics of abdominal aortic aneurysm." Journal of Biomechanics **40**(9): 1887-1902.

Wang, X. C., H. J. Carpenter, M. H. Ghayesh, A. Kotousov, A. C. Zander, M. Amabili and P. J. Psaltis (2023). "A review on the biomechanical behaviour of the aorta." Journal of the Mechanical Behavior of Biomedical Materials **144**: 105922.

Wang, Y. F., D. Joannic, P. Juillion, A. Monnet, P. Delassus, A. Lalande and J. F. Fontaine (2018). "Validation of the Strain Assessment of a Phantom of Abdominal Aortic Aneurysm: Comparison of Results Obtained From Magnetic Resonance Imaging and Stereovision Measurements." Journal of Biomechanical Engineering-Transactions of the Asme **140**(3): 031001.

Wanhainen, A., F. Verzini, I. Van Herzelee, E. Allaire, M. Bown, T. Cohnert, F. Dick, J. van Herwaarden, C. Karkos, M. Koelemay, T. Kölbel, I. Loftus, K. Mani, G. Melissano, J. Powell, Z. Szeberin, E. G. Committee, G. J. de Borst, N. Chakfe, S. Debus, R. Hinchliffe, S. Kakkos, I. Koncar, P. Kolh, J. S. Lindholt, M. de Vega, F. Vermassen, r. Document, M. Björck, S. Cheng, R. Dalman, L. Davidovic, K. Donas, J. Earnshaw, H.-H. Eckstein, J. Golledge, S. Haulon, T. Mastracci, R. Naylor, J.-B. Ricco and H. Verhagen (2019). "Editor's Choice – European Society for Vascular Surgery (ESVS) 2019 Clinical Practice Guidelines on the Management of Abdominal Aorto-iliac Artery Aneurysms." European Journal of Vascular and Endovascular Surgery **57**(1): 8-93.

Wittek, A., F. Alkhatib, R. Vitásek, S. Polzer and K. Miller (2022). "On stress in abdominal aortic aneurysm: Linear versus non-linear analysis and aneurysm rupture risk." International Journal for Numerical Methods in Biomedical Engineering **38**(2): e3554.

Wittek, A., C. Blase, W. Derwich, T. Schmitz-Rixen and C. P. Fritzen (2017). "Characterization of the mechanical behaviour and pathophysiological state of abdominal aortic aneurysms based on 4D ultrasound strain imaging." Optical Methods for Inspection, Characterization, and Imaging of Biomaterials III **10333**: 7-23.

Wittek, A., W. Derwich, C. P. Fritzen, T. Schmitz-Rixen and C. Blase (2018). "Towards non-invasive in vivo characterization of the pathophysiological state and mechanical wall strength of the individual human AAA wall based on 4D ultrasound measurements." Zamm-Zeitschrift Fur Angewandte Mathematik Und Mechanik **98**(12): 2275-2294.